ATLAS NOTE

ATLAS-CONF-2013-069

July 16, 2013

Search for charginos nearly mass-degenerate with the lightest neutralino based on a disappearing-track signature in pp collisions at $\sqrt{s} = 8$ TeV with the ATLAS detector

The ATLAS Collaboration

Abstract

A search is presented for direct chargino production based on a disappearing-track signature using 20.3 fb^{-1} of pp collisions at $\sqrt{s} = 8$ TeV collected with the ATLAS experiment at the LHC. In anomaly-mediated supersymmetry breaking (AMSB) models, the lightest chargino is nearly mass-degenerate with the lightest neutralino and its lifetime is long enough to be detected in the tracking detectors by identifying decays that result in tracks with no associated hits in the outer region of the tracking system. A number of models with supersymmetry also predict charginos with a significant lifetime. This analysis reaches a sensitivity for charginos with a lifetime between 1 ns and 10 ns and masses up to about 500 GeV and for the first time significantly extends the reach of the LEP experiments for charginos with lifetimes > 0.1 ns. No significant excess beyond the background expectation is observed for candidate tracks with large transverse momentum, and constraints on chargino properties are obtained. In the AMSB scenarios, a chargino mass below 270 GeV is excluded at 95% confidence level.

ATLAS-CONF-2013-069
18 July 2013

1 Introduction

Anomaly-mediated supersymmetry breaking (AMSB) models [1, 2], where soft supersymmetry (SUSY) breaking is caused by loop effects, provide a constrained mass spectrum of SUSY particles. One prominent feature of these models is that the lightest supersymmetric particle is the nearly pure neutral wino which is degenerate with the charged wino in mass. The lightest chargino ($\tilde{\chi}_1^{\pm}$) is then slightly heavier than the lightest neutralino ($\tilde{\chi}_1^0$) due to radiative corrections involving electroweak gauge bosons. The typical mass splitting between $\tilde{\chi}_1^{\pm}$ and $\tilde{\chi}_1^0$ ($\Delta m_{\tilde{\chi}_1}$) is $\sim$ 160 MeV, which implies that $\tilde{\chi}_1^{\pm}$ has a considerable lifetime and predominantly decays into $\tilde{\chi}_1^0$ plus a low-momentum ($\sim$ 100 MeV) $\pi^{\pm}$. The mean lifetime ($\tau_{\tilde{\chi}_1^{\pm}}$) of $\tilde{\chi}_1^{\pm}$ is expected to be typically a fraction of a nanosecond. A number of SUSY models, which are motivated by the large value of the Higgs boson mass, also predict charginos with a significant lifetime and their decay to a soft pion and the lightest supersymmetric particle [3–6]. Therefore, some charginos will have decay lengths exceeding a few tens of centimeters at the Large Hadron Collider (LHC). When decaying in the sensitive volume, they are observed as "disappearing tracks" and no or only a few hits in the outer region of the tracking system are associated with their tracks. This article explores AMSB scenarios by searching for charginos with their subsequent decays that result in such disappearing tracks. The electroweak production of charginos has a sizeable cross-section in pp collisions at LHC energies. Chargino-pair and chargino-neutralino associated production processes are identified using additional jets of large transverse momentum (p_{T}) from initial-state radiation ($pp \to \tilde{\chi}_1^{\pm}\tilde{\chi}_1^0 j$ and $\tilde{\chi}_1^{+}\tilde{\chi}_1^{-} j$, where j denotes a jet used to trigger the signal event). The result presented here, based on the 8 TeV collision data, increases the sensitivity compared to the previous ATLAS searches [7, 8] due to the increase of beam energy, integrated luminosity and analysis improvements. The most significant improvement is achieved by enhancing the track reconstruction efficiency for charginos having short decay lengths and analysis improvements. In particular, the efficiency for charginos with $\tau_{\tilde{\chi}_1^{\pm}} \sim 0.2$ ns, predicted for $\Delta m_{\tilde{\chi}_1} \sim 160$ MeV, is around 100 times larger than that in the previous searches. The present analysis also provides sensitivity to a wider range of chargino lifetimes and covers a larger angular acceptance.

2 The ATLAS detector

ATLAS is a multi-purpose detector [9], covering nearly the entire solid angle [1] around the collision point with layers of tracking devices surrounded by a superconducting solenoid providing a 2 T axial magnetic field, a calorimeter system, and a muon spectrometer. The inner detector (ID) provides track reconstruction in the region $|\eta| < 2.5$ and consists of pixel and silicon microstrip (SCT) detectors inside a straw tube transition radiation tracker (TRT). The TRT, of particular importance to this search, covers $|\eta|$ up to 1.0 with its barrel detector, $0.8 < |\eta| < 2.0$ with the endcaps and the radial range 563–1066 mm. The average numbers of pixel, SCT and TRT hits on a track going through the inner detector in the central region are about 3, 8 and 32, respectively. At $\eta \sim 0$ tracks passing through the dead region of the barrel TRT produce no TRT hits. The calorimeter system covers the range of $|\eta| < 4.9$. The electromagnetic calorimeter is a lead/liquid-argon (LAr) detector in the barrel ($|\eta| < 1.475$) and endcap ($1.375 < |\eta| < 3.2$) regions. The hadronic calorimeters are composed of a steel and scintillator barrel ($|\eta| < 1.7$), a LAr/copper endcap ($1.5 < |\eta| < 3.2$), and a LAr forward system ($3.1 < |\eta| < 4.9$) with copper and tungsten absorbers. The muon spectrometer consists of three large superconducting toroids, trigger chambers and precision tracking chambers which provide muon momentum measurements up to $|\eta|$ of 2.7.

[1] ATLAS uses a right-handed coordinate system with its origin at the nominal interaction point (IP) in the center of the detector and the z-axis coinciding with the axis of the beam pipe. The x-axis points from the IP to the center of the LHC ring, and the y-axis points upward. Cylindrical coordinates (r, ϕ) are used in the transverse plane, ϕ being the azimuthal angle around the beam pipe. Pseudorapidity is defined in terms of the polar angle θ as $\eta = -\ln\tan(\theta/2)$.

3 Data and simulated event samples

The data analyzed for this search were recorded in 2012 with the LHC colliding protons at $\sqrt{s} = 8$ TeV. The integrated luminosity, after the application of beam, detector and data quality requirements, corresponds to 20.3 ± 0.6 fb^{-1}, where the luminosity is measured based on the calibration procedure described in Ref. [10] and using the most recent van der Meer scans performed in November 2012 to determine the calibration and its uncertainty.

The analysis makes use of a dedicated topological trigger in order to suppress a huge multijet background: it requires at least one jet with $p_{\mathrm{T}} > 80$ GeV, large missing transverse momentum (its magnitude, $E_{\mathrm{T}}^{\mathrm{miss}}$, above 70 GeV), and $\Delta\phi_{\mathrm{min}}^{\mathrm{jet}-E_{\mathrm{T}}^{\mathrm{miss}}} > 1$, where $\Delta\phi_{\mathrm{min}}^{\mathrm{jet}-E_{\mathrm{T}}^{\mathrm{miss}}}$ indicates the smallest azimuthal separation between the missing transverse momentum and either of the two highest-p_{T} jets with $p_{\mathrm{T}} > 45$ GeV. For the multijet background $\Delta\phi_{\mathrm{min}}^{\mathrm{jet}-E_{\mathrm{T}}^{\mathrm{miss}}}$ peaks at around 0 since a large $E_{\mathrm{T}}^{\mathrm{miss}}$ is usually due to jet mismeasurements and aligned with a high-p_{T} jet, while the signal events cluster $\Delta\phi_{\mathrm{min}}^{\mathrm{jet}-E_{\mathrm{T}}^{\mathrm{miss}}} \approx \pi$.

Simulated Monte Carlo (MC) events are used to assess the experimental sensitivity to given models. The minimal AMSB model is characterized by four parameters: the gravitino mass ($m_{3/2}$), the universal scalar mass (m_0), the ratio of Higgs vacuum expectation values at the electroweak scale ($\tan\beta$), and the sign of the higgsino mass term (μ). A large value of 1 TeV is used for m_0 in order to prevent the appearance of a tachyonic slepton. The production cross-section is determined largely by the wino mass and is largely independent of the other parameters. In this model the wino mass is proportional to $m_{3/2}$. Isasusy from Isajet v7.80 [11] is used to calculate the SUSY mass spectrum and the decay tables. The MC signal samples are produced using Herwig++ 2.5.2 [12] with CTEQ6L1 [13] parton distribution functions (PDFs). All simulated samples used in this article are produced using a detector simulation based on Geant4 [14, 15], and include multiple pp interactions (pile-up) in the triggered and adjacent bunch crossings to model that observed in data. Simulated points with chargino masses ($m_{\tilde{\chi}_1^\pm}$) ranging from 80–600 GeV and various values of the chargino lifetime $\tau_{\tilde{\chi}_1^\pm}$ are generated. In the Geant4 simulation the chargino follows an exponential decay and the branching fraction for the decay $\tilde{\chi}_1^\pm \rightarrow \tilde{\chi}_1^0\pi^\pm$ is set to 100%. Signal cross-sections are calculated at next-to-leading order in α_{s} using Prospino2 [16] as shown in Fig. 1. The nominal cross-section and its uncertainty are taken from an envelope of cross-section predictions using different PDF sets and factorization and renormalization scales, as described in Ref. [17].

4 Reconstruction, object identification and event selection

Standard Model (SM) processes, especially $W^\pm$+jet events which naturally have large $E_{\mathrm{T}}^{\mathrm{miss}}$, can result in final-state kinematics similar to that of the signal. Kinematic selection criteria are applied to ensure high trigger efficiency and to reduce background arising from multijet processes or from electroweak gauge bosons that decay leptonically. At the next stage, the vast majority of SM background events are removed by identifying and demanding a disappearing track in the event.

4.1 Track reconstruction

Charged particle trajectories are reconstructed as tracks in the ID. In order to efficiently make use of particles leaving short tracks, this analysis applies an extra extended track reconstruction which provides pixel-seeded reconstructed tracks in addition to the ATLAS standard tracks. The standard track reconstruction algorithm [18] is a sequence made of two main steps. A first inside-out sequence starts from triplets of three-dimensional space points from the pixel and SCT detectors, and then extends the resulting trajectories outwards by combining other silicon and TRT hits. A second sequence takes the

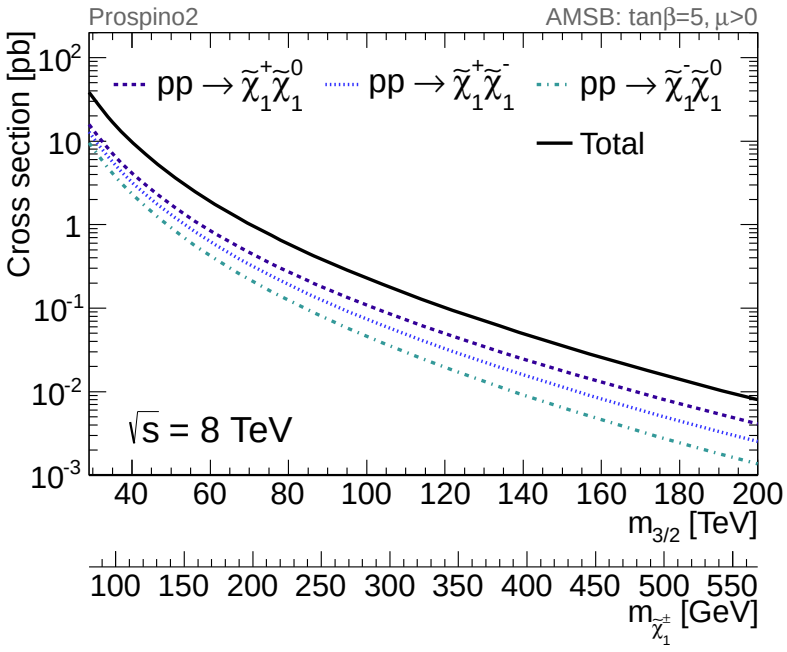

Figure 1: The cross-section for direct chargino production at $\sqrt{s} = 8$ TeV as a function of the gravitino mass $m_{3/2}$. The corresponding chargino mass for each $m_{3/2}$ value is indicated.

remaining TRT hits as seeds and attempts to extend identified trajectories inwards by combining with unused silicon hits. The first sequence is optimized to find primary tracks coming from the interaction point, while the second sequence is optimized for the reconstruction of electrons from photon conversions in the ID volume. The inside-out sequence is of particular interest for finding long-lived chargino trajectories, although it is optimized for the reconstruction of stable particles which leave long tracks in the ID, and in particular, only reconstructs tracks with a minimum of seven silicon hits. In order to increase the acceptance of the track reconstruction and especially the chargino track reconstruction efficiency at low radius, a third sequence is applied. This sequence proceeds using leftover silicon hits from the two previous tracking sequences and reconstructs tracks with a minimum of three pixel hits, while no SCT or TRT hits are required. The outward extension then follows; SCT and TRT hits are attached if they lie along the track trajectory. The tracks reconstructed by the third sequence are used only to select disappearing-track candidates.

4.2 Event reconstruction

The primary vertex [19] is required to have at least five associated tracks. When more than one such vertex is found, the vertex with the largest $\sum |p_{\mathrm{T}}|^2$ of the associated tracks is chosen. Jets are reconstructed using the anti-k_t algorithm [20] with a distance parameter of 0.4. The inputs to the jet reconstruction algorithm are topological calorimeter energy clusters seeded by cells with energy significantly above the noise level. Jet energies are then calibrated back to the particle-level [21]. Reconstructed jets must satisfy the requirements of $p_{\mathrm{T}} > 20$ GeV and $|\eta| < 2.8$. Electron candidates are reconstructed from energy clusters in the electromagnetic calorimeter matched to a track in the ID. Electrons are then required to fulfil "loose" identification requirements, as described in Ref. [22], and transverse energy, $E_{\mathrm{T}} > 10$ GeV, and $|\eta| < 2.47$. Muon candidates are formed by matching ID tracks with either a complete track or a track segment reconstructed in the muon spectrometer [23]. Furthermore, muons are required to have at least one hit in the innermost layer of the pixel detector ($N_{\mathrm{b-layer}}$) if crossing an active module of that

layer, more than one pixel hit (N_{pixel}), at least six SCT hits (N_{SCT}), $p_{\text{T}} > 10$ GeV and $|\eta| < 2.4$.

Following the object reconstruction described above, overlaps between jets and leptons are resolved. First, any jet candidate lying within a distance of $\Delta R \equiv \sqrt{(\Delta\eta)^2 + (\Delta\phi)^2} = 0.2$ of an electron is discarded. Then, any lepton candidate within a distance of $\Delta R < 0.4$ of any surviving jet is discarded.

The calculation of $E_{\text{T}}^{\text{miss}}$ is based on the transverse momenta of jets and lepton candidates described above and all calorimeter energy clusters that are not associated to such objects [24].

4.3 Kinematic selection

Following the event reconstruction described above, selection requirements to reject non-collision background events, given in Ref. [21], are applied to jets. In order to suppress the background events from W/Z + jets and top-pair production processes, events are then discarded if they contain any electron or muon candidates (lepton veto). Events containing muons are further suppressed by requiring no tracks with $p_{\text{T}} > 10$ GeV reconstructed in the muon spectrometer. The candidates are finally required to have $E_{\text{T}}^{\text{miss}} > 90$ GeV, at least one jet with $p_{\text{T}} > 90$ GeV and $\Delta\phi_{\text{min}}^{\text{jet}-E_{\text{T}}^{\text{miss}}} > 1.5$ for the two highest p_{T} jets with $p_{\text{T}} > 45$ GeV. The trigger selection is > 98% efficient for signal events satisfying these selection requirements.

4.4 Selection of disappearing tracks

The tracks originating from charginos are expected to have a high transverse momentum p_{T}, to be isolated and to have few associated hits in the outer region of the ID. The TRT detector in particular provides substantial discrimination from penetrating stable charged particles by requiring a small number of hits on the track. Therefore, candidate tracks of decaying charginos are required to fulfil the following criteria:

(I) The track must have $N_{\text{pixel}} \geq 3$, $N_{\text{b-layer}} \geq 1$ if crossing an active module of the innermost pixel layer, $N_{\text{SCT}} \geq 2$, $|d_0| < 0.1$ mm and $|z_0 \sin\theta| < 0.5$ mm, where d_0 and z_0 are the transverse and longitudinal impact parameters with respect to the primary vertex.

(II) The track reconstruction must be of good quality, meeting the following requirements: it must have a track fit χ^2-probability of > 10%, no hits formed in a single pixel row of which the readout is shared with another pixel, and no hits missing in active silicon modules along the trajectory between the first and last hit of the track.

(III) The track must be isolated: it must fulfil $p_{\text{T}}^{\text{cone40}}/p_{\text{T}} < 0.04$, where $p_{\text{T}}^{\text{cone40}}$ is the sum of p_{T} of all tracks with $p_{\text{T}} > 400$ MeV, $|d_0| < 1.5$ mm and $|z_0 \sin\theta| < 1.5$ mm within a cone of $\Delta R = 0.4$ around the track. There must also be no jets having p_{T} above 45 GeV within a cone of $\Delta R = 0.4$ around the track.

(IV) The candidate track must have p_{T} above 15 GeV, and must be the highest-p_{T} isolated track in the event.

(V) The candidate track must point to the active regions of the TRT detector ($0.1 < |\eta| < 1.9$).

(VI) The number of hits in the TRT detector associated to the track (N_{TRT}), calculated by counting hits lying on the extrapolated track, must be fewer than five.

Criteria (I) and (II) are applied in order to ensure well-reconstructed primary tracks. Criteria (III) and (IV) are employed to select chargino tracks that are isolated and have the highest p_{T} in most cases. Criterion (V) is used to ensure the coverage of the TRT active region and enhance the rejection of background

tracks. Criterion (VI) helps to remove the majority of background tracks in SM processes, as shown in Fig. 2; SM charged particles traversing the TRT detector typically have the number of TRT hits $N_{\mathrm{TRT}} \simeq 32$, and conversely, charginos decaying before reaching the TRT detector are expected to have $N_{\mathrm{TRT}} = 0$. Hereafter, "high-p_{T} isolated track selection" and "disappearing-track selection" indicate criteria (I)–(V) and (I)–(VI), respectively.

Making use of short-length tracks and the whole TRT detector for the background track rejection extends the sensitive decay volume inwards and enlarges the signal acceptance in η. This results in a better sensitivity for charginos especially with small lifetime in comparison with that in the previous search [8] based on the 7 TeV collision data. Fig. 3 shows the tracking efficiency with the disappearing-track selection as a function of the radius and η of the decay; it is fully efficient for charginos that reach the first SCT layer and decay before reaching the TRT detector, and also largely independent of $m_{\tilde{\chi}_1^\pm}$. A summary of kinematic selection criteria, disappearing-track requirements, and the data reduction are given in Table 1.

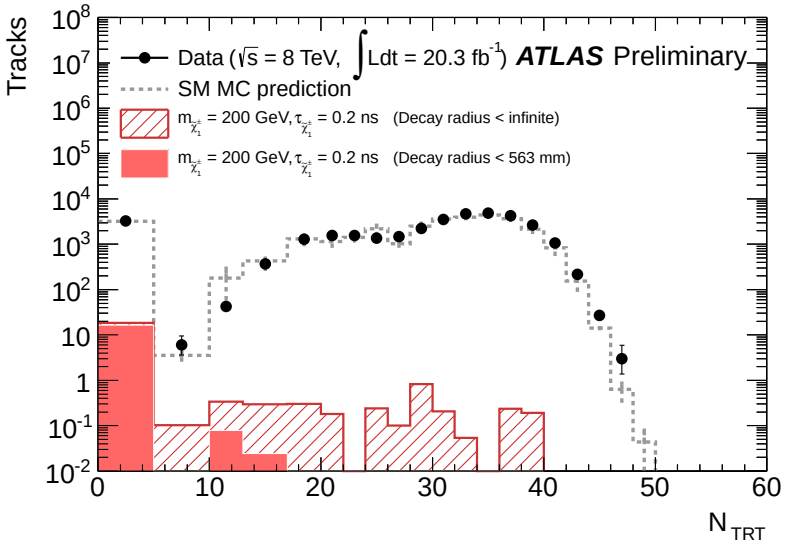

Figure 2: Number of TRT hits (N_{TRT}) for data and signal MC events ($m_{\tilde{\chi}_1^\pm} = 200$ GeV, $\tau_{\tilde{\chi}_1^\pm} = 0.2$ ns) with the high-p_{T} isolated track selection. The expectation from SM MC events is also shown. The solid colored histogram shows the expected distribution for charginos with a decay radius < 563 mm while the hatched histogram shows it for all charginos for these mass and lifetime values.

5 Estimate of the p_{T} spectrum of background tracks

There are three primary sources of tracks from background processes that mimic the disappearing tracks signature: charged hadrons interacting with material in the ID (interacting-hadron tracks), prompt electrons or muons failing to satisfy their identification criteria (lepton tracks) and low-p_{T} charged particles whose p_{T} is largely mismeasured (p_{T}-mismeasured tracks). Interacting-hadron and electron tracks are responsible for the background for the range of approximately $p_{\mathrm{T}} < 50$ GeV, and p_{T}-mismeasured tracks for $p_{\mathrm{T}} > 100$ GeV. A small contribution from muon tracks is expected throughout the full p_{T} range. The contribution of charged-hadron decays is significantly smaller than that of interacting hadrons, therefore, such a background source is neglected. A background estimation based on the MC simulation has difficulty in accurately describing the properties of these background tracks. Therefore, the background contribution to the disappearing-track candidates is estimated using techniques that do not rely on the

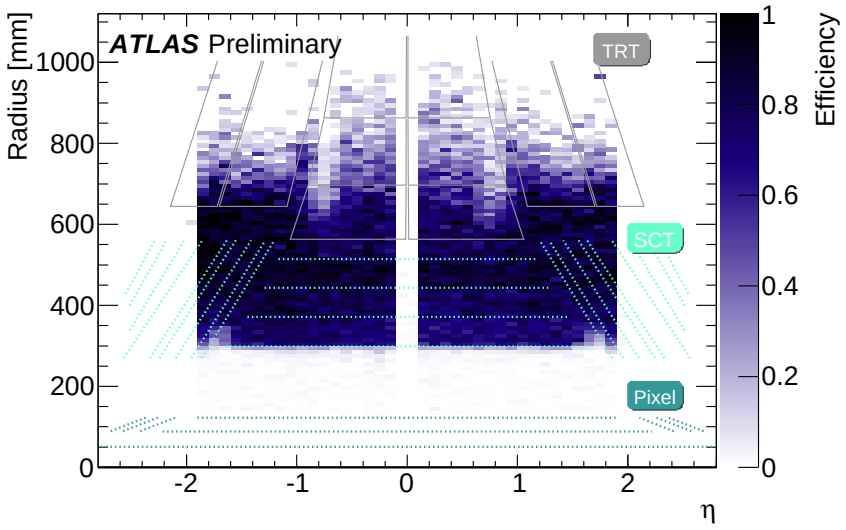

Figure 3: The efficiency for decaying charginos with the disappearing-track selection. Vertical and horizontal axes are the radius and η of the decay, respectively. Sensitive layers and areas of the pixel, SCT and TRT detectors are also indicated in the figure.

Selection requirement	Observed events	Expected signal events (efficiency [%])
Quality requirements and trigger	20479553	1873 (8.8)
Jet cleaning	18627508	1867 (8.8)
Lepton veto	12485944	1827 (8.6)
Leading jet $p_{\mathrm{T}} > 90$ GeV	10308840	1571 (7.4)
$E_{\mathrm{T}}^{\mathrm{miss}} > 90$ GeV	6113773	1484 (7.0)
$\Delta\phi_{\mathrm{min}}^{\mathrm{jet}-E_{\mathrm{T}}^{\mathrm{miss}}} > 1.5$	5604087	1444 (6.8)
High-p_{T} isolated track selection	34379	21.9 (0.10)
Disappearing-track selection	3256	18.4 (0.087)

Table 1: Summary of selection requirements and data reduction for data and expected signal events ($m_{\tilde{\chi}_1^\pm} = 200$ GeV, $\tau_{\tilde{\chi}_1^\pm} = 0.2$ ns). The signal selection efficiencies are also shown in parentheses. Signal efficiencies are low at the first stage due to the trigger based on initial state radiation.

MC simulation. Each of the three types of background tracks shows a distinctive p_{T} spectrum; a simultaneous fit is performed for signal and background yields using the observed p_{T} spectrum and templates of background-track p_{T} spectra produced from dedicated control data samples. The p_{T} spectra of the first two background types are obtained in the same way as in Ref. [8].

5.1 Interacting hadron tracks

Charged hadrons, mostly charged pions, can interact with material in the ID and their tracks can be misidentified as disappearing tracks. The p_{T} shape of interacting hadron tracks is obtained from that of non-interacting hadron tracks. In the p_{T} range above 15 GeV, where inelastic interactions dominate, the interaction rate has nearly no p_{T}-dependence [25]. By adopting the same kinematic selection criteria as those for the signal and ensuring a penetration through the TRT detector by requiring $N_{\mathrm{TRT}} > 25$, a data sample of non-interacting hadron tracks is obtained. A pure control data sample is ensured by

requiring associated calorimeter activity and removing the contamination from electron and muon tracks (described below) and any chargino signal. The following requirements are applied: $E_{\mathrm{T}}^{\mathrm{cone40}} > 7.5$ GeV and $\sum_{\Delta R<0.4} E_{\mathrm{T}}^{\mathrm{clus}} / p_{\mathrm{T}}^{\mathrm{track}} > 0.4$, where $E_{\mathrm{T}}^{\mathrm{cone40}}$ is the transverse calorimeter energy deposited in a cone of $\Delta R < 0.4$ around the track, excluding E_{T} of the calorimeter cluster matched to the track, $\sum_{\Delta R<0.4} E_{\mathrm{T}}^{\mathrm{clus}}$ is the sum of cluster energies in a cone of $\Delta R < 0.4$ around the track, and $p_{\mathrm{T}}^{\mathrm{track}}$ is the track p_{T}.

In most cases interacting hadrons have associated calorimeter activity which can be used to form jets. Therefore, after the selection requirements, the contribution of this background to the disappearing-track candidates having $p_{\mathrm{T}} > 100$ GeV is negligibly small.

5.2 Leptons failing to satisfy identification criteria

A fraction of charged leptons ($\ell \equiv e$ or μ) lose their momenta in the ID due to scattering with material or large bremsstrahlung. Such leptons are unlikely to be correctly identified (hence surviving the lepton veto) and may be classified as disappearing tracks.

In order to estimate the lepton-track background, a control data sample is defined by requiring the same kinematic selection requirements as for the signal search sample, while requiring one lepton that fulfils its identification criteria and the isolated track selection criteria. The p_{T} spectrum of leptons without any identification requirements is obtained by applying a correction for the identification efficiency. The p_{T} distribution of lepton background tracks is then estimated by multiplying this distribution by the probability ($\mathcal{P}_{\ell}^{\mathrm{dis}}$) of failing to satisfy the loose identification criteria (hence being retained in the signal search sample) and passing the disappearing-track selection criteria for leptons. The electron and muon components are considered separately.

For the measurement of $\mathcal{P}_{\ell}^{\mathrm{dis}}$, a tag-and-probe method is applied to $Z \to \ell\ell$ events collected with unprescaled single-lepton triggers and by requiring a Z candidate with reconstructed invariant mass within ± 5 GeV of the Z mass. Tag-leptons are required to be well isolated from jets and to fulfil the lepton identification criteria. Probe-leptons are selected without any identification requirements but with exactly the same high-p_{T} isolated track selection criteria used for chargino candidate tracks. The probability $\mathcal{P}_{\ell}^{\mathrm{dis}}$ is given by the fraction of events in which the probe-lepton passes the disappearing-track selection criteria; it ranges between 10^{-2}–10^{-4} for electrons and 10^{-4}–10^{-5} for muons. Statistical uncertainties and uncertainties on the identification efficiency are considered in deriving the estimated p_{T} spectra and their uncertainties.

5.3 p_{T}-mismeasured tracks

The background contribution to disappearing-track candidates with $p_{\mathrm{T}} > 100$ GeV originates primarily from p_{T}-mismeasured tracks. Combinations of wrong space-points in the procedure of track-seed finding or outward-extension of trajectories can result in anomalously high values of p_{T} especially for short-length tracks. Simulation studies indicate that the p_{T} spectrum of such tracks depends little on the reconstructed d_0 or production process. Fig. 4 shows the p_{T} spectrum of disappearing tracks with different d_0 values in a multijet-enriched data sample collected with single-jet triggers and requirements of $E_{\mathrm{T}}^{\mathrm{miss}} < 90$ GeV and no leptons: the contamination from interacting-hadron and lepton tracks are expected to be very small in the range $p_{\mathrm{T}} > 50$ GeV or $|d_0| > 1$ mm. The p_{T} shape of p_{T}-mismeasured tracks with $|d_0| < 0.1$ mm is assumed to be the same as that of similarly mismeasured tracks with 1 mm $< |d_0| <$ 10 mm. A sample with a nearly-pure p_{T}-mismeasured track contribution can be obtained with the same requirements as for the signal tracks, while requiring 1 mm $< |d_0| <$ 10 mm. The p_{T} shape is finally determined by a fit to a functional form x^{-a} ($x \equiv p_{\mathrm{T}}^{\mathrm{track}}$), where $a = 1.78 \pm 0.05$ is obtained.

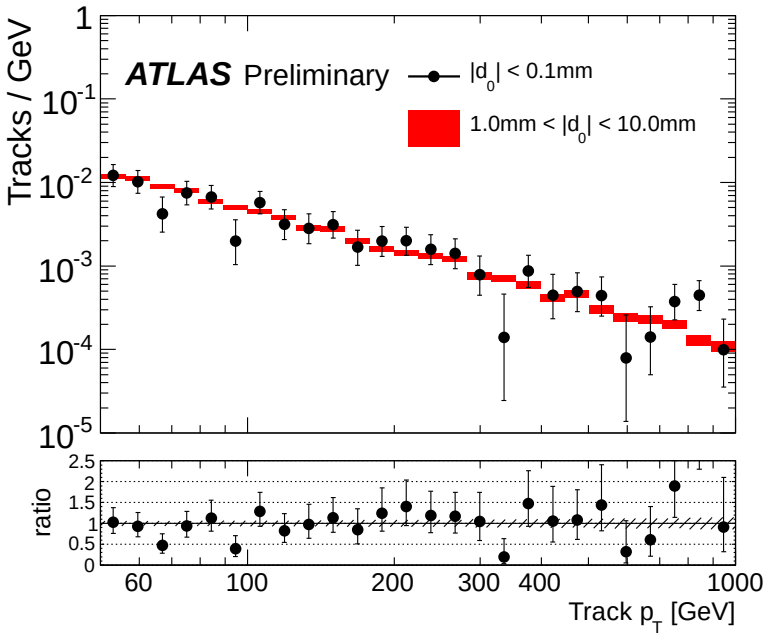

Figure 4: p_{T} distributions of disappearing tracks with impact parameter ranges $|d_0| < 0.1$ mm and 1 mm $< |d_0| <$ 10 mm in the multijet-enriched data sample, normalized to unity. The ratio between the two distributions is also shown at the bottom of the figure. The error bars and band in the ratio plot indicate the statistical uncertainties of each sample.

6 Estimate of systematic uncertainties

The sources of systematic uncertainty on the signal expectation are the following: the theoretical cross-section, parton radiation model, jet energy scale (JES) and resolution (JER), trigger efficiency, pile-up modeling, track reconstruction efficiency, and the integrated luminosity. The contributions of each systematic uncertainty in the signal yield are summarized in Table 2 for two reference signal samples.

Theoretical uncertainties on the signal cross-section, already described in Section 3, range from 6% to 8% depending on $m_{\tilde{\chi}_1^\pm}$. The uncertainties on the modeling of high-p_{T} jets, originating from initial- and final-state radiation, are estimated by varying generator tunes in the simulation as well as by generator-level studies carried out on samples produced with an additional jet in the matrix-element method using MadGraph5 [26] and Pythia6 [27]. By adopting PDF tunes that provide less and more radiation and taking the maximum deviation from the nominal tune, the uncertainty due to jet radiation is evaluated. The uncertainty arising from the matching of matrix elements with parton showers is evaluated by varying the default value of the matching parameter [28] up and down by a factor of 2. The resulting changes are combined in quadrature and yield an uncertainty of 10–17% depending on $m_{\tilde{\chi}_1^\pm}$. The uncertainties on the JES and JER result in a variation of the signal selection efficiency which is assessed according to Ref. [21], and an uncertainty of 3–6% is assigned. An uncertainty due to the trigger efficiency is estimated to be 4.5% by taking the difference between data and MC in a $W \to \mu\nu$ sample. The uncertainty originating from the pile-up modeling in the simulation is evaluated by weighting simulated samples so that the average number of pile-up interactions is varied by ± 10%, which yields a 0.5% uncertainty on the signal efficiency. The ID material affects the track reconstruction efficiency. An uncertainty of 2% is assigned from Ref. [29] to take into account differences in the tracking efficiency between data and MC related to the detector material description in the simulation. The uncertainty on the integrated luminosity

is ±2.8%. It is derived, following the same methodology as that detailed in Ref. [10], from a preliminary calibration of the luminosity scale derived from beam-separation scans performed in November 2012.

Systematic uncertainties on the background p_{T} shapes and normalizations arising from statistical uncertainties of the control data samples and uncertainties on the lepton identification efficiencies are also considered in deriving the results (see Section 7). In order to account for a possible bias induced by the d_0 requirement in the data control sample of p_{T}-mismeasured tracks, an additional uncertainty is assigned by taking the difference between the a-parameter given in Section 5.3 and the value 1.82 ± 0.07 derived using SM background MC events remaining after the selection requirements.

Source	200 GeV	300 GeV
(Theoretical uncertainty)		
Cross-section	6.4	6.8
(Uncertainty on the acceptance)		
Modeling of initial/final-state radiation	14.5	16.4
JES/JER	3.9	6.0
Trigger efficiency	4.5	4.5
Pile-up modeling	0.5	0.5
Track reconstruction efficiency	2.0	2.0
Luminosity	2.8	2.8
Sub-total	16.1	18.4

Table 2: Summary of systematic uncertainties [%] on the expected number of signal events for $m_{\tilde{\chi}_1^\pm} = 200$ and 300 GeV.

7 Fit to the p_{T} spectrum of disappearing tracks

The signal hypothesis with a given value of $m_{\tilde{\chi}_1^\pm}$ and $\tau_{\tilde{\chi}_1^\pm}$ is tested based on an extended maximum likelihood fit to the p_{T} spectrum of the disappearing-track candidates. The likelihood function for the track p_{T} consists of a probability density function for the signal and four for the different backgrounds derived in Section 5. In the fit, the yields of the signal, interacting-hadron and p_{T}-mismeasured tracks are left free. The yields of electron and muon background tracks are constrained to their estimated values within the uncertainties. The effects of systematic uncertainties on the yields and the shape parameters describing the p_{T} shapes of the background tracks are also incorporated in the likelihood function.

The number of observed events having a high-p_{T} disappearing track above a given threshold and the expectation for the background, derived by the background-only fit in the p_{T} range below 75 GeV, are given in Table 3. No significant deviations from the background expectations are found. The probability (p_0 value) that a background-only experiment is more signal-like than observed and the model-independent upper limit on the visible cross-section ($\sigma_{\mathrm{vis}}^{95\%}$) at 95% confidence level (CL) are also given in the table. Fig. 5 shows the p_{T} distribution for the selected data events compared to the background model derived by the background-only fit: the best-fit values for the yields of interacting hadrons, electron tracks, muon tracks and p_{T}-mismeasured tracks are 2187 ± 71, 852 ± 35, 23 ± 8 and 212 ± 33, respectively. Three selected examples for the signal are also shown in the figure.

An excess with a corresponding significance of $\sim 2\sigma$ is observed at p_{T} around 90 GeV. Detailed investigation of the events in this region show no peculiarities or significant differences in event kinematics or track properties compared to candidates in nearby track-p_{T} regions. The discrepancy is also not consistent with any of the signal hypotheses studied in this paper. For the models considered, high-p_{T} tracks are expected and the best expected sensitivity derives from the region with p_{T} above 200 GeV, where a deficit is observed as reported in Table 3.

	> 75 GeV	> 100 GeV	> 150 GeV	> 200 GeV
Observed events	59	36	19	13
Expected events	48.5 ± 12.3	37.1 ± 9.4	24.6 ± 6.3	18.0 ± 4.6
p_0 value	0.17	0.41	0.46	0.44
Observed $\sigma_{\text{vis}}^{95\%}$ [fb]	1.76	1.02	0.62	0.44
Expected $\sigma_{\text{vis}}^{95\%}$ [fb]	$1.42^{+0.50}_{-0.39}$	$1.05^{+0.37}_{-0.28}$	$0.67^{+0.27}_{-0.19}$	$0.56^{+0.23}_{-0.16}$

Table 3: Numbers of observed and expected background events as well as probability that a background-only experiment is more signal-like than observed (p_0) and the model-independent upper limit on the visible cross-section ($\sigma_{\text{vis}}^{95\%}$) at 95% CL.

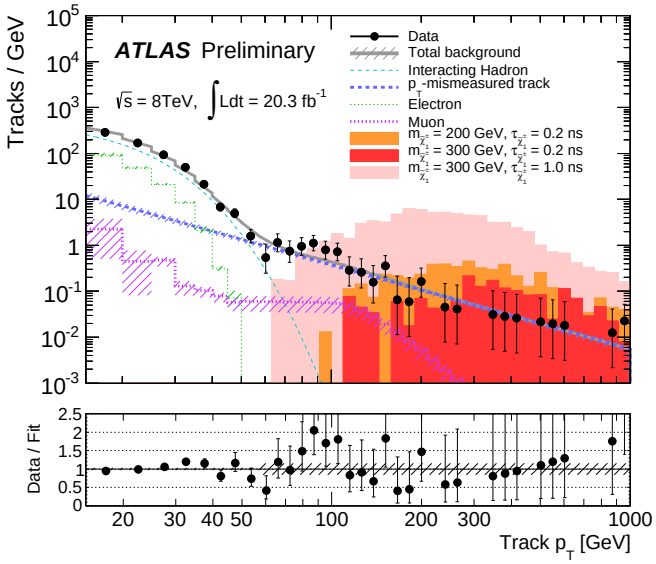

Figure 5: The p_{T} distribution of disappearing-track candidates. The solid circles show data and lines show each background track-p_{T} spectrum obtained by the background-only fit. The resulting uncertainties on the p_{T} spectrum for each background are indicated by the error bands. The signal expectations are also shown. The ratio between data and the background track-p_{T} spectrum is shown at the bottom of the figure.

Events with two disappearing-track candidates, being particularly sensitive to chargino-pair production with a long lifetime, are also explored. One candidate event is found, however, the event lacks high-p_{T} candidates (30 GeV and 18 GeV).

8 Results

In the absence of a signal, constraints are set on $m_{\tilde{\chi}_1^\pm}$ and $\tau_{\tilde{\chi}_1^\pm}$. The upper limit on the production cross-section for a given $m_{\tilde{\chi}_1^\pm}$ and $\tau_{\tilde{\chi}_1^\pm}$ at 95% CL is set by a point where the CL of the "signal+background" hypothesis, based on the profile likelihood ratio [30] and the *CLs* prescription [31], falls below 5% when scanning the CL along various values of signal strength. The constraint on the $\tau_{\tilde{\chi}_1^\pm}$–$m_{\tilde{\chi}_1^\pm}$ parameter space is shown in Fig. 6. The expected limit is set by the median of the distribution of 95% CL limits calculated by pseudo-experiments with the expected background and no signal, where the systematic parameters are varied according to their systematic uncertainties. The regions excluded by the LEP2 searches [32–35]

and the previous ATLAS search [8] are indicated. The analysis is not performed for signals having $\tau_{\tilde{\chi}_1} > 10$ ns (corresponding $\Delta m_{\tilde{\chi}_1}$ being below the charged pion mass) because a significant fraction of charginos would traverse the ID before decaying, thereby reducing the event selection efficiency. In these scenarios the charginos are considered as stable particles and the main search tool would be to look for tracks with anomalous ionization energy loss [36]. In comparison with the previous result, the sensitivity to charginos having $\tau_{\tilde{\chi}_1^\pm} < 1$ ns is significantly improved and the exclusion reach is extended by ~ 200 GeV.

Fig. 7 shows the constraint on the $\Delta m_{\tilde{\chi}_1}$–$m_{\tilde{\chi}_1^\pm}$ parameter space of the minimal AMSB model; the expected 95% CL exclusion reaches 245^{+25}_{-30} GeV for $\Delta m_{\tilde{\chi}_1} \sim 160$ MeV. The limits on $\tau_{\tilde{\chi}_1^\pm}$ are converted into limits on $\Delta m_{\tilde{\chi}_1}$ following Ref. [37]. The theoretical calculation of $\Delta m_{\tilde{\chi}_1}$ at two-loop level [38] is also indicated in the figure. A new limit of $m_{\tilde{\chi}_1^\pm} < 270$ GeV (corresponding $\Delta m_{\tilde{\chi}_1}$ and $\tau_{\tilde{\chi}_1^\pm}$ being ~ 160 MeV and ~ 0.2 ns, respectively) at 95% CL is set in the AMSB models.

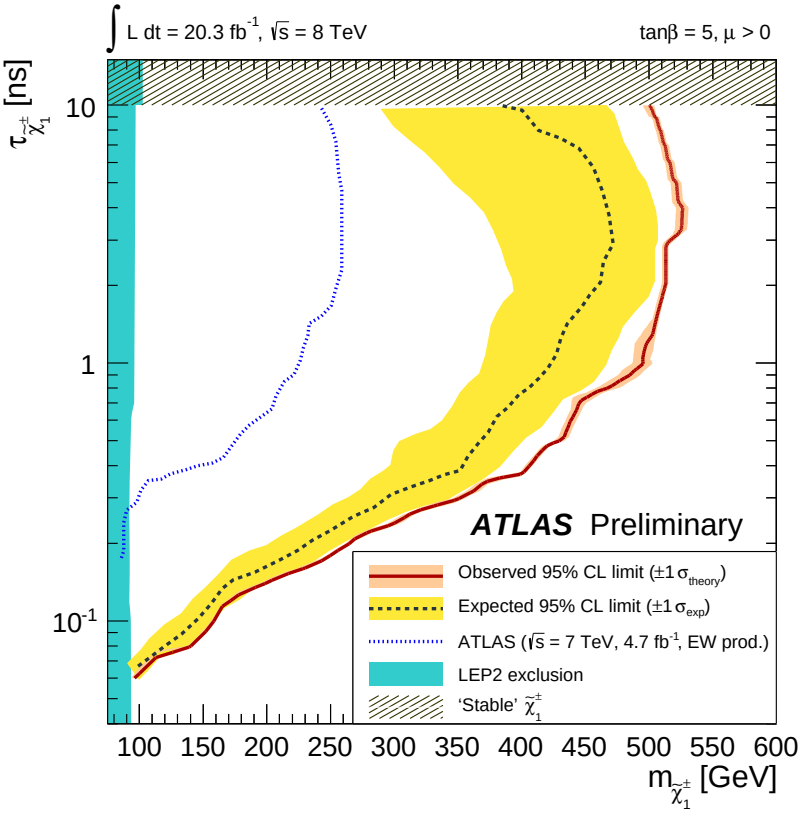

Figure 6: The constraint on the $\tau_{\tilde{\chi}_1^\pm}$–$m_{\tilde{\chi}_1^\pm}$ space for $\tan\beta = 5$ and $\mu > 0$. The black dashed line shows the expected limits at 95% CL, with the surrounding shaded bands indicating the 1σ exclusions due to experimental uncertainties. Observed limits are indicated by the solid bold contour representing the nominal limit and the surrounding shaded bands are obtained by varying the cross-section by the theoretical scale and PDF uncertainties. The previous result from Ref. [8] and the combined LEP2 exclusion at 95% CL are also shown on the left by the dotted line and the shaded region, respectively.

9 Conclusions

The results from a search for charginos nearly mass-degenerate with the lightest neutralino based on the high-p_{T} disappearing-track signature are presented. The analysis is based on 20.3 fb^{-1}of pp collisions

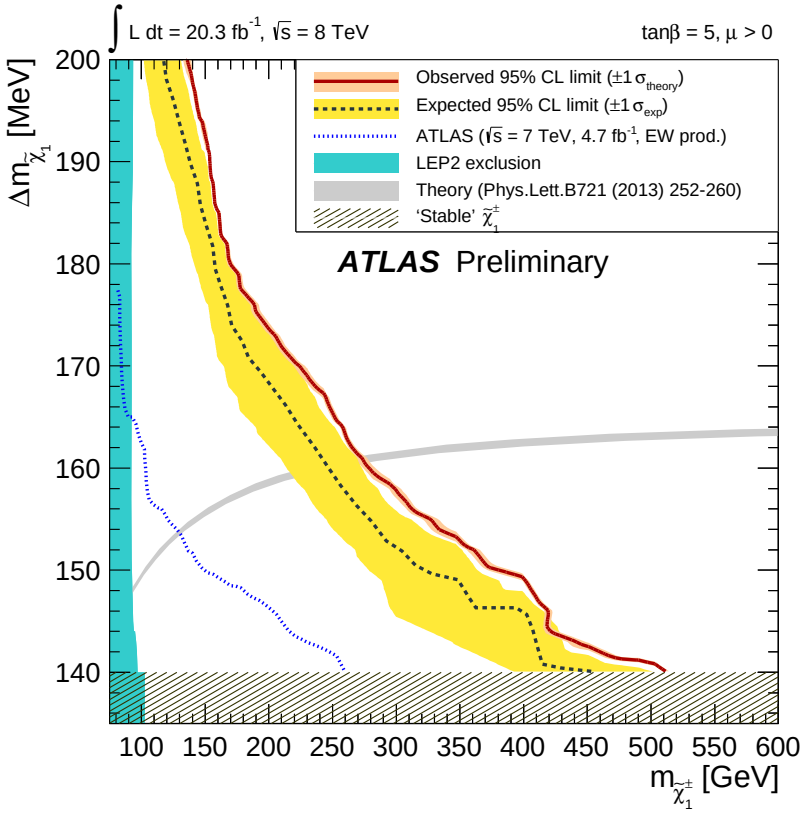

Figure 7: The constraint on the $\Delta m_{\tilde{\chi}_1}$–$m_{\tilde{\chi}_1^\pm}$ space of the AMSB model for $\tan\beta = 5$ and $\mu > 0$. The dashed line shows the expected limits at 95% CL, with the surrounding shaded bands indicating the 1σ exclusions due to experimental uncertainties. Observed limits are indicated by the solid bold contour representing the nominal limit and the surrounding shaded bands are obtained by varying the cross-section by the theoretical scale and PDF uncertainties. The combined LEP2 exclusion at 95% CL and the theoretical calculation are also shown by the shaded regions on the left and in the middle, respectively. Charginos in the lower shaded region could have significantly longer lifetime values for which this analysis has no sensitivity as the chargino does not decay within the tracking volume.

at $\sqrt{s} = 8$ TeV collected by the ATLAS experiment at the LHC. The p_{T} spectrum of observed candidate tracks is found to be consistent with the expectation from SM background processes, and no indication of decaying charginos is observed. Constraints on the chargino mass, the mean lifetime and the mass splitting are set, which are valid for most scenarios in which the lightest supersymmetric particle is the nearly pure neutral wino. In the AMSB models, a chargino having a mass below 270 GeV is excluded at 95% CL.

References

[1] G. F. Giudice, M. A. Luty, H. Murayama, and R. Rattazzi, *Gaugino Mass without Singlets*, JHEP **12** (1998) 027, arXiv:hep-ph/9810442.

[2] L. Randall and R. Sundrum, *Out of this world supersymmetry breaking*, Nucl. Phys. **B557** (1999) 79–118, arXiv:hep-th/9810155.

[3] M. Ibe, S. Matsumoto, and T. T. Yanagida, *Pure Gravity Mediation with $m_{3/2}$ = 10-100 TeV*, Phys.Rev. **D85** (2012) 095011, arXiv:1202.2253 [hep-ph].

[4] L. J. Hall, Y. Nomura, and S. Shirai, *Spread Supersymmetry with Wino LSP: Gluino and Dark Matter Signals*, JHEP **1301** (2013) 036, arXiv:1210.2395 [hep-ph].

[5] A. Arvanitaki, N. Craig, S. Dimopoulos, and G. Villadoro, *Mini-Split*, JHEP **1302** (2013) 126, arXiv:1210.0555 [hep-ph].

[6] N. Arkani-Hamed, A. Gupta, D. E. Kaplan, N. Weiner, and T. Zorawski, *Simply Unnatural Supersymmetry*, arXiv:1212.6971 [hep-ph].

[7] ATLAS Collaboration, *Search for anomaly-mediated supersymmetry breaking with the ATLAS detector based on a disappearing-track signature in pp collisions at $\sqrt{s}$ = 7 TeV*, Eur. Phys. J. **C72** (2012) 1993, arXiv:1202.4847 [hep-ex].

[8] ATLAS Collaboration, *Search for direct chargino production in anomaly-mediated supersymmetry breaking models based on a disappearing-track signature in pp collisions at $\sqrt{s}$ = 7 TeV with the ATLAS detector*, JHEP **1301** (2013) 131, arXiv:1210.2852 [hep-ex].

[9] ATLAS Collaboration, *The ATLAS Experiment at the CERN Large Hadron Collider*, JINST **3** (2008) S08003.

[10] ATLAS Collaboration, *Improved luminosity determination in pp collisions at sqrt(s) = 7 TeV using the ATLAS detector at the LHC*, arXiv:1302.4393 [hep-ex].

[11] F. E. Paige, S. D. Protopopescu, H. Baer, and X. Tata, *ISAJET 7.69: A Monte Carlo event generator for pp, $\bar{p}p$, and e^+e^- reactions*, arXiv:hep-ph/0312045 [hep-ph].

[12] M. Bahr, S. Gieseke, M. Gigg, D. Grellscheid, K. Hamilton, et al., *Herwig++ Physics and Manual*, Eur. Phys. J. **C58** (2008) 639–707, arXiv:0803.0883 [hep-ph].

[13] J. Pumplin et al., *New generation of parton distributions with uncertainties from global QCD analysis*, JHEP **07** (2002) 012, arXiv:hep-ph/0201195.

[14] GEANT4 Collaboration, S. Agostinelli et al., *GEANT4: A simulation toolkit*, Nucl. Instrum. Meth. **A506** (2003) 250–303.

[15] ATLAS Collaboration, *The ATLAS Simulation Infrastructure*, Eur. Phys. J. **C70** (2010) 823–874, arXiv:1005.4568 [physics.ins-det].

[16] W. Beenakker, R. Hopker, M. Spira, and P. Zerwas, *Squark and gluino production at hadron colliders*, Nucl. Phys. **B492** (1997) 51–103, arXiv:hep-ph/9610490 [hep-ph].

[17] M. Kramer, A. Kulesza, R. van der Leeuw, M. Mangano, S. Padhi, et al., *Supersymmetry production cross sections in pp collisions at $\sqrt{s}$ = 7 TeV*, arXiv:1206.2892 [hep-ph].

[18] T. Cornelisen *et al.*, *The new ATLAS track reconstruction (NEWT)*, J. Phys. Conf. Ser **119** (2008) 032014.

[19] ATLAS Collaboration, *Performance of primary vertex reconstruction in proton-proton collisions at $\sqrt{s}$ =7 TeV in the ATLAS experiment*, ATLAS-CONF-2010-069. http://cdsweb.cern.ch/record/128134.

[20] M. Cacciari, G. P. Salam, and G. Soyez, *The anti-k_t jet clustering algorithm*, JHEP **04** (2008) 063, arXiv:0802.1189 [hep-ph].

[21] ATLAS Collaboration, *Jet energy measurement with the ATLAS detector in proton-proton collisions at $\sqrt{s}$ = 7 TeV*, Eur.Phys.J. **C73** (2013) 2304, arXiv:1112.6426 [hep-ex].

[22] ATLAS Collaboration, *Electron performance measurements with the ATLAS detector using the 2010 LHC proton-proton collision data*, Eur. Phys. J. **C72** (2012) 1909, arXiv:1110.3174 [hep-ex].

[23] ATLAS Collaboration, *Muon reconstruction efficiency in reprocessed 2010 LHC proton-proton collision data recorded with the ATLAS detector*, ATLAS-CONF-2011-063. https://cds.cern.ch/record/1345743.

[24] ATLAS Collaboration, *Performance of Missing Transverse Momentum Reconstruction in Proton-Proton Collisions at 7 TeV with ATLAS*, Eur. Phys. J. **C72** (2012) 1844, arXiv:1108.5602 [hep-ex].

[25] Particle Data Group Collaboration, K. Nakamura et al., *Review of particle physics*, J. Phys. **G37** (2010) 075021. Corresponding data may be found at pages 398–399.

[26] J. Alwall, M. Herquet, F. Maltoni, O. Mattelaer, and T. Stelzer, *MadGraph 5 : Going Beyond*, JHEP **1106** (2011) 128, arXiv:1106.0522 [hep-ph].

[27] T. Sjöstrand, S. Mrenna, and P. Z. Skands, *PYTHIA 6.4 Physics and Manual*, JHEP **0605** (2006) 026, arXiv:hep-ph/0603175.

[28] J. Alwall, S. Hoche, F. Krauss, N. Lavesson, L. Lonnblad, et al., *Comparative study of various algorithms for the merging of parton showers and matrix elements in hadronic collisions*, Eur. Phys. J. **C53** (2008) 473–500, arXiv:0706.2569 [hep-ph].

[29] ATLAS Collaboration, *Measurements of underlying-event properties using neutral and charged particles in pp collisions at 900 GeV and 7 TeV with the ATLAS detector at the LHC*, Eur. Phys. J. **C71** (2011) 1636, arXiv:1103.1816 [hep-ex].

[30] G. Cowan, K. Cranmer, E. Gross, and O. Vitells, *Asymptotic formulae for likelihood-based tests of new physics*, Eur. Phys. J. **C71** (2011) 1554, arXiv:1007.1727 [physics.data-an].

[31] A. L. Read, *Presentation of search results: The CL(s) technique*, J. Phys. **G28** (2002) 2693–2704.

[32] ALEPH Collaboration, A. Heister et al., *Search for charginos nearly mass degenerate with the lightest neutralino in e^+e^- collisions at center-of-mass energies up to 209 GeV*, Phys. Lett. **B533** (2002) 223–236, arXiv:hep-ex/0203020 [hep-ex].

[33] OPAL Collaboration, G. Abbiendi et al., *Search for nearly mass degenerate charginos and neutralinos at LEP*, Eur. Phys. J. **C29** (2003) 479–489, arXiv:hep-ex/0210043 [hep-ex].

[34] DELPHI Collaboration, J. Abdallah et al., *Search for SUSY in the AMSB scenario with the DELPHI detector*, Eur. Phys. J. **C34** (2004) 145–156, arXiv:hep-ex/0403047 [hep-ex].

[35] LEP2 SUSY Working Group. http://lepsusy.web.cern.ch/lepsusy/www/inoslowdmsummer02/charginolowdm_pub.html.

[36] ATLAS Collaboration, *Searches for heavy long-lived sleptons and R-Hadrons with the ATLAS detector in pp collisions at* $\sqrt{s} = 7$ *TeV*, Phys.Lett. **B720** (2013) 277–308, arXiv:1211.1597 [hep-ex].

[37] C. Chen, M. Drees, and J. Gunion, *Addendum/erratum for 'searching for invisible and almost invisible particles at* e^+e^- *colliders' [hep-ph/9512230] and 'a nonstandard string/SUSY scenario and its phenomenological implications' [hep-ph/9607421]*, arXiv:hep-ph/9902309 [hep-ph].

[38] M. Ibe, S. Matsumoto, and R. Sato, *Mass Splitting between Charged and Neutral Winos at Two-Loop Level*, Phys.Lett. **B721** (2013) 252–260, arXiv:1212.5989 [hep-ph].

Appendix: Auxiliary plots

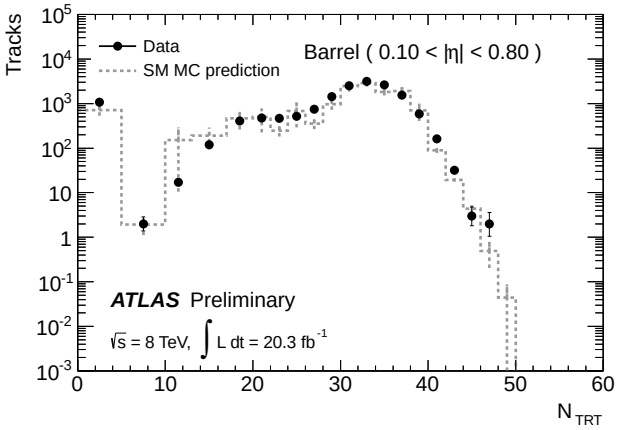

(a) $0.1 < |\eta| \leq 0.8$

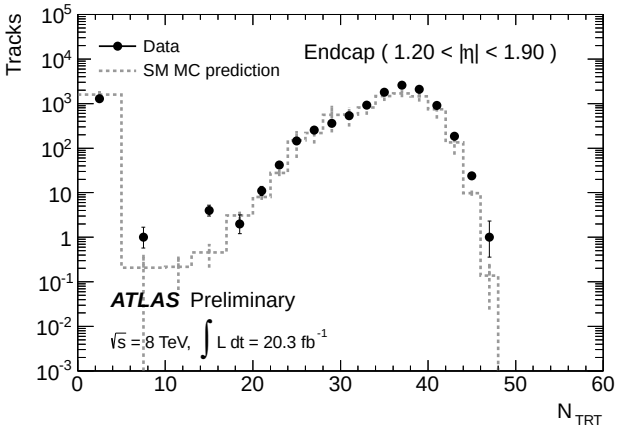

(b) $1.2 < |\eta| \leq 1.9$

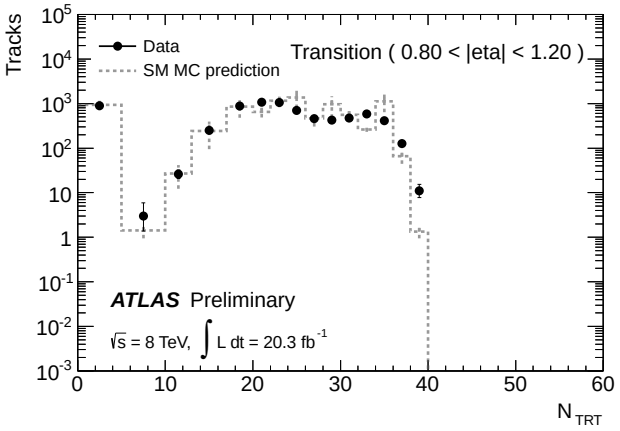

(c) $0.8 < |\eta| \leq 1.2$

Figure 8: The N_{TRT} distributions of high-p_{T} isolated tracks pointing to the TRT barrel (a), endcap (b) and transition (c) regions. The SM MC expectation is also shown.

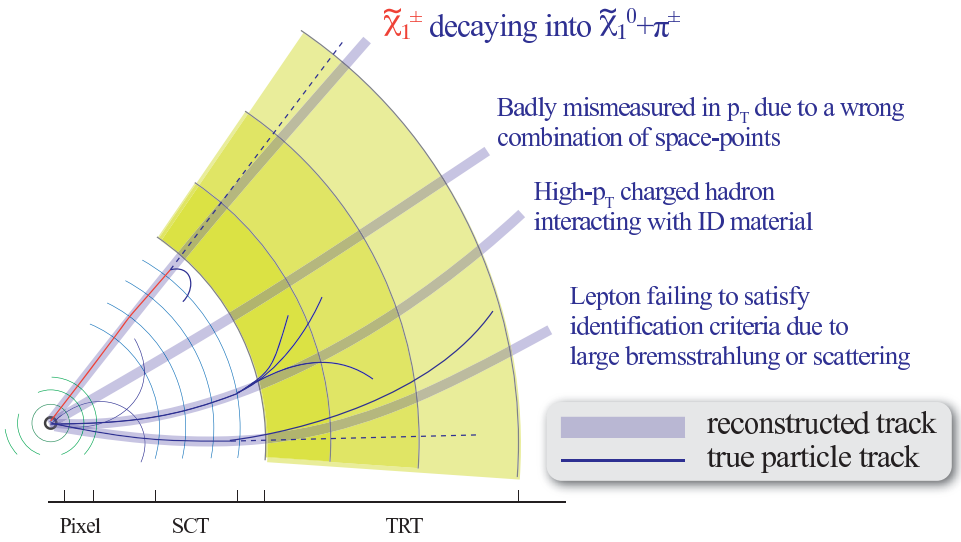

Figure 9: Origins of high-p_{T} disappearing tracks

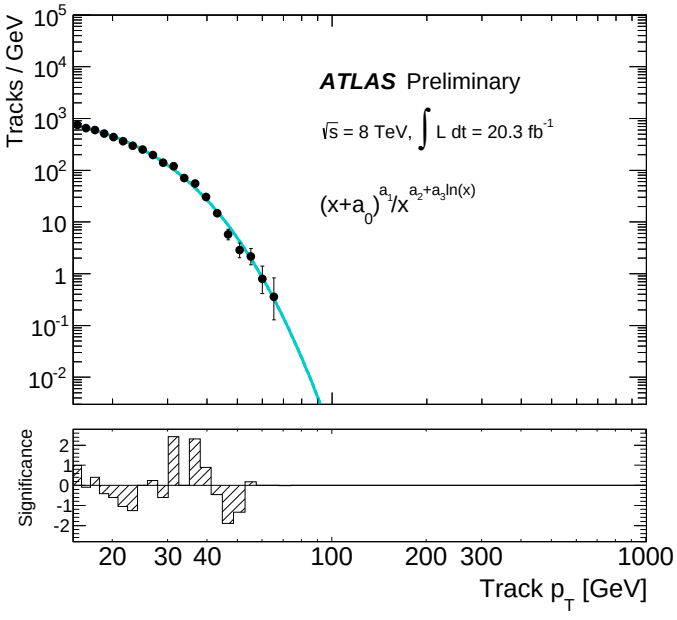

Figure 10: The p_{T} distribution of hadron track background control sample. The data and the fitted shape are shown by solid circles and a line, respectively. The significance of the data-model difference on a bin-by-bin basis is also shown at the bottom of the figure.

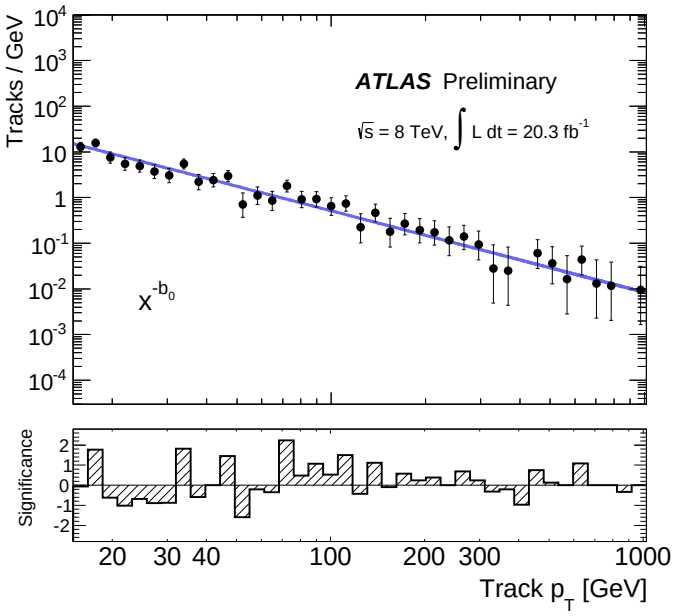

Figure 11: The p_{T} distribution of p_{T}-mismeasured track control sample. The data and the fitted shape are shown by solid circles and a line, respectively. The significance of the data-model difference on a bin-by-bin basis is also shown at the bottom of the figure.

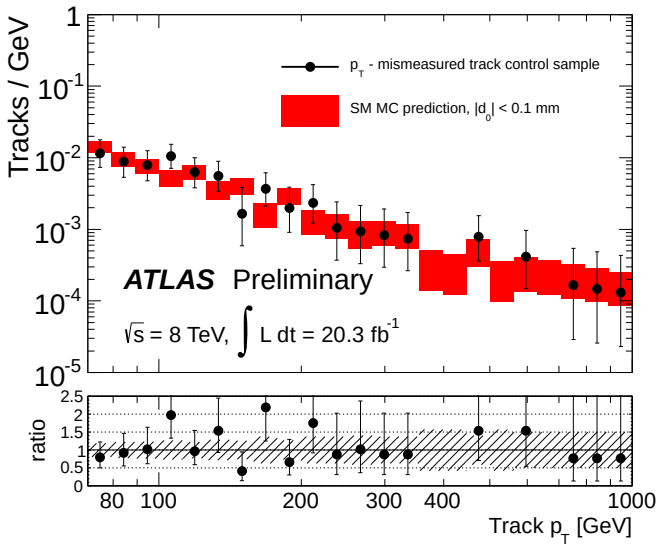

Figure 12: The p_{T} distribution of p_{T}-mismeasured track control sample and the SM MC background prediction. The error bars and band indicate the statistical uncertainties of each sample.

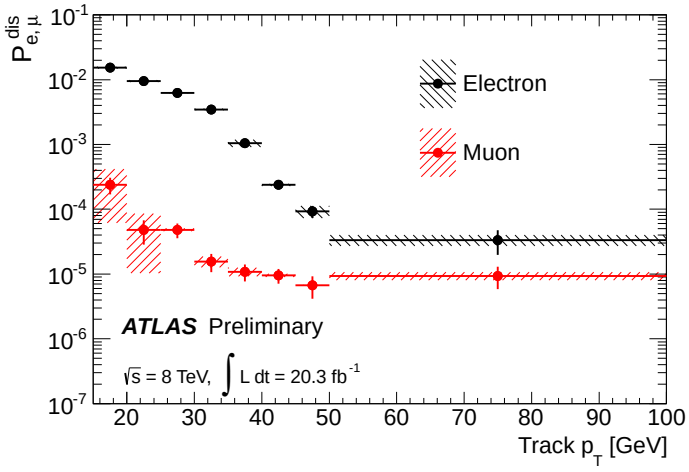

Figure 13: The probability of failing to satisfy the identification criteria and passing the disappearing-track selection criteria for electrons and muons.

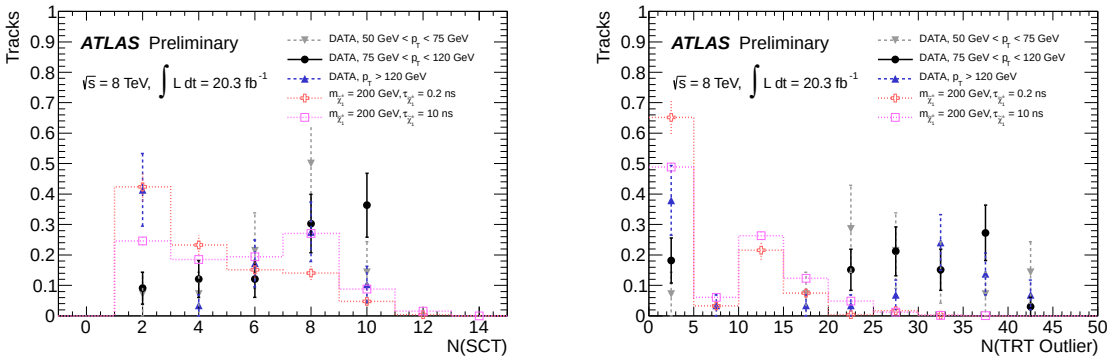

(a) N_{SCT}

(b) The number of TRT outliers

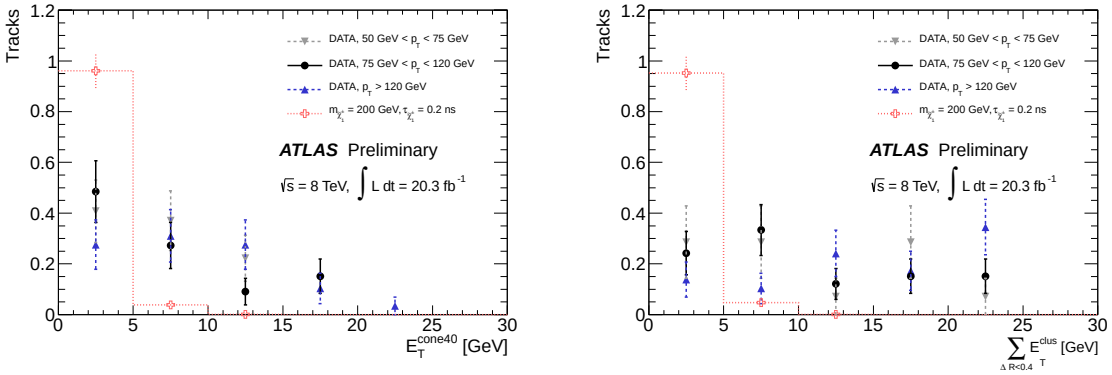

(c) $E_{\mathrm{T}}^{\mathrm{cone40}}$

(d) $\sum_{\Delta R<0.4} E_{\mathrm{T}}^{\mathrm{clus}}$

Figure 14: Comparison of track properties between the excess region and nearby track-p_{T} regions. The signal expectation is also shown.